

JGR Solid Earth

RESEARCH ARTICLE

10.1029/2023JB027292

Key Points:

- Different influential factors have significant impacts on the initiation pressure
- Existence of natural fractures, high injection rates and heterogeneity degrees increase the geometrical complexity of fractures
- Low-viscosity fluid combined with a high injection rate leads to a complex fracture network in low-permeability heterogeneous formation

Correspondence to:

M. Wang,
mrwang@tsinghua.edu.cn

Citation:


Zhu, W., Chen, Z., He, X., Tian, Z., & Wang, M. (2023). Numerical investigation of influential factors in hydraulic fracturing processes using coupled discrete element-lattice Boltzmann method. *Journal of Geophysical Research: Solid Earth*, 128, e2023JB027292. <https://doi.org/10.1029/2023JB027292>

Received 18 JUN 2023
Accepted 23 AUG 2023

Author Contributions:

Conceptualization: Weiwei Zhu, Zhiqiang Chen, Moran Wang
Data curation: Xupeng He
Funding acquisition: Moran Wang
Investigation: Zhiqiang Chen, Xupeng He, Moran Wang
Methodology: Weiwei Zhu, Zhiqiang Chen, Moran Wang
Project Administration: Moran Wang
Supervision: Moran Wang
Validation: Zhiguo Tian
Writing – original draft: Weiwei Zhu
Writing – review & editing: Zhiqiang Chen, Xupeng He, Zhiguo Tian, Moran Wang

Numerical Investigation of Influential Factors in Hydraulic Fracturing Processes Using Coupled Discrete Element-Lattice Boltzmann Method

Weiwei Zhu^{1,2} , Zhiqiang Chen³, Xupeng He⁴, Zhiguo Tian¹, and Moran Wang¹ 

¹Department of Engineering Mechanics, Tsinghua University, Beijing, China, ²Key Laboratory of Shale Gas and Geoengineering, Institute of Geology and Geophysics, Chinese Academy of Sciences, Beijing, China, ³Petroleum Exploration and Production Research Institute, SINOPEC, Beijing, China, ⁴EXPEC Advanced Research Center, Saudi Aramco, Dhahran, Kingdom of Saudi Arabia

Abstract Hydraulic fracturing is widely used to stimulate unconventional reservoirs, but a systematic and comprehensive investigation into the hydraulic fracturing process is insufficient. In this work, a discrete element-lattice Boltzmann method is implemented to simulate the hydro-mechanical behavior in a hydraulic fracturing process. Different influential factors, including treatment parameters (injection rates and fluid viscosity), formation parameters (in situ stress states and natural fractures) and rock properties (heterogeneity of rock strengths and rock permeability), are considered and their impacts on the initiation and propagation of hydraulic fractures are evaluated. A higher injection rate, increased viscosity, and larger in situ stress will lead to an increase in the initiation pressure. Conversely, higher formation permeability and a greater degree of heterogeneity in bond strengths will result in a decrease in the initiation pressure. The complexity of generated fractures is significantly influenced by the injection rate and degree of heterogeneity. However, fluid viscosity, in situ stress states, and formation permeability individually do not affect the geometrical complexity. Shear displacement can occur during a hydraulic fracturing process due to increased pore pressure and variations in in situ stress caused by injected fluid. Low-viscosity fluid with a high injection rate can have a significant pressure buildup and generate complex fracture networks in low-permeability heterogeneous formations. Natural fractures can significantly impact the complexity of generated fractures, while more in-depth research is required regarding complex natural fracture distributions.

Plain Language Summary Hydraulic fracturing technique is essential for the development of unconventional reserves, such as shale gas/oil and geothermal reservoirs. To optimize field operations and properly estimate the stimulation reservoir volume, it is necessary to investigate the impact of influential factors. In this work, we adopt a numerical scheme (DEM-LBM) to investigate the process in detail and consider as many factors as possible, including treatment parameters (injection rates and fluid viscosity), formation parameters (in situ stress states and preexisting natural fractures), and rock properties (heterogeneity of rock strengths and rock permeability). The impacts of those influential factors on the initiation and propagation of hydraulic fractures are evaluated. We find that all factors have a significant impact on fracture initiation pressure. However, the complexity of generated fractures is mainly affected by injection rates and heterogeneity degrees of rock strengths. The combination of low-viscosity fluid and a high injection rate can result in the generation of a much more complex fracture network in a low-permeability heterogeneous formation. The existence of natural fractures can significantly influence the complexity of the generated fracture networks. Further research on natural fracture networks is feasible based on the foundation established in this work.

1. Introduction

Hydraulic fracturing refers to the process of injecting highly pressurized liquid into a well to break up bedrock formations, which is vastly implemented in stimulating unconventional reservoirs, for example, shale oil, shale gas, and enhanced geothermal systems (Gandossi & Von Estorff, 2013; Pruess, 2006). During the hydraulic fracturing process, a complex fracture network is formed, comprising both newly generated hydraulic fractures and reactivated natural fractures. This network is known as the stimulated reservoir volume (SRV), which plays a crucial role in determining the ultimate fluid production from low-permeability formations.

However, the hydraulic fracturing process occurs in the deep subsurface and cannot be observed directly. Current available techniques, such as microseismic monitoring, tiltmeter measurement, and electromagnetic imaging, cannot reveal the detailed internal structure of SRV. Zhu et al. (2022) proposed a novel method to explicitly represent SRV using discrete fracture networks coupled with a given failure criterion. However, their model greatly simplifies the hydraulic fracturing process, and an in-depth investigation of the possible influential factors is necessary.

To investigate the initiation and propagation in the hydraulic fracturing process, numerous theoretical, experimental, and numerical works have been presented. Classic theoretical works include the Perkins-Kern-Nordgren (PKN) model (Nordgren, 1972; Perkins & Kern, 1961) and the Kristianovich-Geertsma-de Klerk (KGD) model (Geertsma & De Klerk, 1969; Khristianovic & Zheltov, 1955). The classic models typically simplify fracture geometries and formation properties, such as assuming a penny-shaped fracture for the KGD model and a constant height for the PKN model. They also assume an infinite homogeneous isotropic linear elastic formation for both models. Later, Marder et al. (2015) extended the analytical model to incorporate fracture networks. Analytical models provide convenient estimates of fracture lengths or widths, but they do not provide detailed information about the hydraulic fracturing process. For instance, it is challenging to account for rock heterogeneity using analytical models.

Hydraulic fracturing is a complex process and many factors can influence the initiation and geometry of hydraulic fractures, like formation parameters (e.g., in situ stress and preexisting natural fractures), treatment parameters (e.g., injection rate and fluid viscosity), and rock properties (e.g., rock strength heterogeneity and rock permeability) (De Pater & Beugelsdijk, 2005; Fazio et al., 2021; Liu et al., 2018; Zeng & Roegiers, 2002; Zhuang et al., 2019). Experiments under triaxial and true triaxial stress conditions are widely adopted to mimic the actual geostress states (Huang & Liu, 2017; Zhao et al., 2019). The acoustic emission method is used to monitor the hydraulic fracturing process (Goodfellow et al., 2015; Stanchits et al., 2014), but similar to the microseismicity method in the field, detailed morphology information of fractures is not available. CT scanning is widely adopted to observe the fracture morphologies inside rock samples (Kumari et al., 2018; Liu et al., 2018). However, CT scanning method is limited to the resolution and long operation time, which is difficult to capture the real-time variations of fracture initiation and propagation process. Although lab results provide helpful insights, they are destructive experiments and cannot use an identical rock sample in each test. Therefore, it is almost impossible to investigate the impact of individual factor through a strict factor control. 3D-printed samples can reproduce the same rock samples and optical visualization is available (Liu et al., 2016), but it is both time-consuming and financially expensive to conduct a comprehensive investigation of influential factors through experiments. In addition, the printing materials are usually far different from actual rocks in terms of physical and mechanical properties.

In contrast to experiments, numerical simulations provide better control over factors and enable the investigation of the impact of individual or multiple factors. The hydraulic fracturing process is a strongly coupled hydro-mechanical process. For the mechanical part, several continuum and mesoscale numerical methods are used to simulate fracture initiation and propagation. The continuum methods mainly include the boundary element method (Cheng et al., 2022; Olson & Taleghani, 2009), extended finite element method (Dahi-Taleghani & Olson, 2011; Mohammadnejad & Khoei, 2013), and phase field methods (Heider, 2021; Wilson & Landis, 2016). However, the continuum method usually involves high requirements for mesh quality and complicated treatments for complex boundary conditions. Therefore, the mesoscale numerical method is also widely used to simulate mechanical deformation, which mainly refers to the discrete element method (DEM). DEM directly describes the mechanical displacements and interactions of discontinues particles (Cundall & Strack, 1979). For the fluid dynamics part, the assumption of lubrication flow is usually used since a fracture has a width significantly smaller than its length. The finite volume method (FVM) and finite element method (FEM) can be used to discretize and solve the flow equations and couple with mechanical part (Lecampion, 2009; Peirce & Detournay, 2009). Munjiza et al. (1995) proposed a combined Finite-Discrete Element Method (FDEM) and further extended to advanced fluid-solid solver, FSIS (Fluid-Solid Interaction Solver) (Munjiza et al., 2020) and HOSS (Hybrid Optimization Software Suite) (Knight et al., 2020). The FDEM is robust and well adopted by many research institutes and universities (Knight et al., 2020; Lei et al., 2019; Yan et al., 2016). Compared with FVM and FEM, the lattice Boltzmann method (LBM) has several advantages, such as simple calculation procedures, convenient implementation of parallel computation, and simple treatment of complex geometries. In addition, through the Chapman-Enskog theory, the Navier-Stokes equations can be derived from the Boltzmann equation (S. Chen &

Doolen, 1998). Therefore, the LBM method can solve the Navier-Stokes equations and overcome the possible inaccuracy caused by the lubrication flow assumption. Coupled DEM-LBM method is a good option for simulating the hydro-mechanical coupling process (Z. Chen & Wang, 2017; Z. Chen et al., 2020; Galindo-Torres, 2013a; Galindo-Torres et al., 2012).

In this work, a DEM-LBM scheme is proposed, which can simulate the hydraulic fracturing process and consider various factors. The impacts of individual and multiple factors on the hydraulic fracturing process are evaluated, which is essential to better understand the formation of a complex SRV in the subsurface. Section 2 introduces detailed information about the coupled method. Impacts of different factors on fracture initiation and propagation are demonstrated in Section 3. In Section 4, we discuss the limitation of the method and possible improvements. Important conclusions are summarized in Section 5.

2. Methods and Materials

2.1. A DEM-LBM Scheme for the Simulation of Hydraulic Fracturing Process

A DEM-LBM method is proposed in this work to simulate the coupled hydro-mechanical process. The numerical framework is further developed from the multi-physics simulation software MECHSYS developed by Galindo-Torres (2013a) and extension of the software developed by Z. Chen and Wang (2017), Z. Chen et al. (2018, 2020). DEM treats materials as an assembly of discrete particles, which are represented by polyhedrons. Interactions between particles are approximated with linear contact and bonding models (Galindo-Torres et al., 2012).

A threshold value on the total strain, denoted as ϵ_{th} , is provided as the criterion of fracture initiation:

$$|\vec{\epsilon}_n| + |\vec{\epsilon}_t| \geq \epsilon_{th}, \quad (1)$$

where $\vec{\epsilon}_n$ and $\vec{\epsilon}_t$ are the normal and tangential strain caused by the displacement of adjacent particle faces.

A broken bond is classified as a shear failure when its shear strain exceeds the normal strain. Similarly, a tensile failure occurs when the tensile strain surpasses the shear strain. It is important to note that the terms “shear” and “tensile” fractures used here do not imply that they have pure shear or tensile displacement. Rather, the classification is based on the dominant displacement type. A similar classification is adopted in Shimizu et al. (2011) and Z. Chen and Wang (2017).

The LBM is implemented to calculate the fluid flow. Considering the accuracy and computation efficiency, a D3Q15 model is adopted in this work and the corresponding evolution equation is:

$$f_i(\vec{x} + \vec{e}_i \delta t, t + \delta t) = f_i(\vec{x}, t) - \frac{\delta t}{\tau} (f_i(\vec{x}, t) - f_i^{eq}(\vec{x}, t)), \quad i = 0, 1, 2, \dots, 14, \quad (2)$$

where f_i and f_i^{eq} are the density distribution function and the corresponding equilibrium distribution in the i th discrete velocity direction, \vec{e}_i , δt is the time step adopted in the simulation, and τ is the relaxation time. Through the Chapman-Enskog analysis, the pressure can be obtained:

$$p = \frac{1}{3} \rho c^2 \quad (3)$$

The physical pressure difference with proper conversion factors can be calculated by:

$$\Delta p^* = \frac{1}{3} \Delta \rho \frac{\delta^2 x^*}{\delta^2 t^*} \quad (4)$$

where δx^* and δt^* are the physical length of the grid size and physical time step used in the simulation.

An immersed boundary method (IBM) is applied to incorporate the fluid-solid interactions (Z. Chen & Wang, 2017; Noble & Torczynski, 1998). The basic logic behind the IBM method is that the fluid flow is simulated in the whole domain including the particles. For fluid inside a particle, a body force is inserted to make the fluid have the same rigid movement as the particle and the no-slip boundary condition is fulfilled for the external fluid flow. A fluid-solid interaction term Ω_i^{fs} is added in the standard LBM evolution equation.

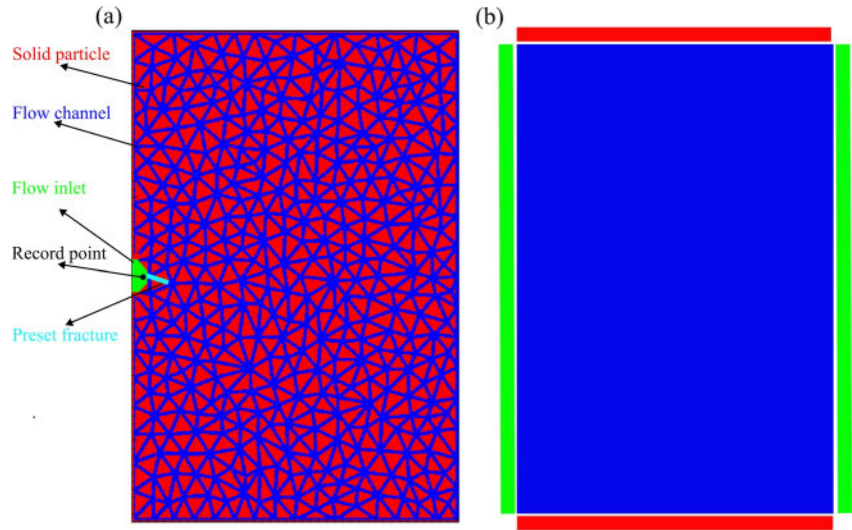


Figure 1. Calculation domain with a length of 6 cm, a width of 4 cm, and a thickness of 1.28 mm.

$$f_i(\vec{x} + \vec{e}_i\delta t, t + \delta t) = f_i(\vec{x}, t) + (1 - B)\left\{-\frac{\delta t}{\tau}(f_i - f_i^{eq})\right\} + B\Omega_i^{fs}, \quad (5)$$

where B is a weighting parameter, which is a function of τ and the solid volume fraction γ :

$$B = \frac{\gamma(\tau/\delta t - 1/2)}{(1 - \gamma) + (\tau/\delta t - 1/2)}, \quad (6)$$

where γ is defined as the ratio of the solid volume over the lattice volume. When $\gamma = 0$, there are no solids in the corresponding fluid lattice. When $\gamma = 1$, the lattice is fully occupied by the solid phase. When $B = 0$, corresponding to $\gamma = 0$ (fluid lattice), the evolution equation degenerates to the standard one. The γ value is also correlated with the rock permeability, and by adjusting the γ values, the impact of different rock permeability is analyzed.

In Appendix A and B, a gravity-driven Poiseuille flow in a slit and a Brazilian test are used to validate the correctness of LBM and DEM schemes.

2.2. Simulation Setup

The simulation model considered is a rectangular plate with a width of 4.0 cm, length of 6.0 cm, and thickness of 1.28 mm. The solid particles are shown in red in Figure 1a with a total number of 741.

The solid particles are eroded and dilated to form “potential” channels for the fluid flow (shown in blue in Figure 1), which can also be regarded as the visualized links between particles. Fractures are modeled through the breakage of those cohesive links between discrete elements, but they cannot cross particles. The solid volume fraction γ is used to control the initial permeability of the flow domain in the LBM lattice. For the whole flow domain, there is a predefined γ controlling the initial permeability of the matrix, which can be used to mimic the leakage of injected fluid to formation in reality. Before the formation of fractures, the “potential” channels have an initial γ value, and after fracture formation, the γ value reduces to zero. A small cave on the left side is assigned as the fluid inlet and the initial γ value is zero. A preset fracture is denoted in Figure 1a, which mimics the perforation process in reality and helps to initiate the hydraulic fracture. The detailed simulation parameters are listed in Table 1.

Table 1
Input Parameters for the DEM-LBM Simulation

Parameter	Value
Normal contact stiffness, K_n	1.0×10^6 N/m
Tangential contact stiffness, K_t	1.0×10^6 N/m
Normal elastic modulus, B_n	2.0×10^6 (Pa)
Tangential elastic modulus, B_t	4.2×10^6 (Pa)
Bond strength, c_{th}	0.01 (–)
Fluid density, ρ_f^*	1.0×10^3 (kg/m ³)
Lattice size in LBM, δ_x^*	1.0×10^{-4} (m)
Time step in DEM/LBM, δ_t^*	1.0×10^{-6} (s)

Four rectangular plates on each side of the domain are added to implement different stresses on the horizontal (left-right) and vertical (top-bottom) directions, shown in Figure 1b. The horizontal and vertical plates have a length of 4.0×10^{-2} and 6.0×10^{-2} m. The width and height of plates are the same as the thickness of the particle, 1.28×10^{-3} m. There is a constant flow-rate condition for the inlet and a fixed pressure is assigned on the right side of the domain. All the other boundaries are set as solid.

Since the DEM is only conditionally stable, the time step should be small enough to reach the convergence. The critical time step is a function of the particle mass, its stiffness, and its arrangement (O'Sullivan & Bray, 2004). To ensure the convergence, the time step fulfills the criterion below (Galindo-Torres et al., 2012):

$$\Delta t_{critical} = 0.1 \sqrt{\frac{M_{min}}{C_{nmax} + B_{nmax}}}, \quad (7)$$

where M_{min} is the minimum mass of all particles, C_{nmax} and B_{nmax} are the maximum normal contact and bond stiffness of all particles, respectively. From Equation 7, a larger value of the particle stiffness requires a smaller time step. In this work, the heterogeneity of rock strengths is considered, which focuses more on the variations of rock strengths instead of actual strength values. Therefore, the stiffness and modulus values are reduced to increase the time step as shown in Table 1, which makes the simulation computationally affordable (Yousefi & Ng, 2017).

If the bond strengths of all particles are the same, it will lead to a homogeneous rock sample. However, real rock samples are always heterogeneous because of different mineral compositions and cement materials. Therefore, the heterogeneous bond strengths are more appropriate for real rocks and it is one of the influential factors investigated in this work. The Weibull distribution is widely adopted to describe heterogeneous bond strengths for brittle rocks (Z. Chen & Wang, 2017; Van Mier et al., 2002):

$$f(\epsilon_{th}) = \frac{m}{\epsilon_{th}^0} \left(\frac{\epsilon_{th}}{\epsilon_{th}^0} \right)^{m-1} \exp\left(-\left(\frac{\epsilon_{th}}{\epsilon_{th}^0}\right)^m\right), \quad (8)$$

where ϵ_{th}^0 is the average bond strength threshold and is set as 0.01 in this work. m is the shape parameter, describing the heterogeneity degree of the bond strength. An infinitely large m corresponds to a homogeneous structure, while a low value of m indicates a heterogeneous structure.

The influential parameters investigated in this work also include the injection rate and in situ stress states. To properly choose the injection rate and the stress levels, we conducted a Buckingham analysis (Buckingham, 1915) with the following steps and scaled our simulation parameters with parameters in actual experiments.

- Choose possible variables: tensile strength S , viscosity of fluid ν , particle size l , injection rate q , fluid density ρ . In total, the number of variables is 5;
- Find variables with repeating units: particle size l , injection rate q , fluid density ρ . Therefore, the number of dimensions is 3 and the basis of fundamental units are T (time), L (distance), and M (mass). Therefore, there should be two independent dimensionless parameters (π_1 and π_2) concerning fluid viscosity ν and tensile strength S .
- The first dimensionless parameter π_1 :

$$\pi_1 = \nu \times l^a \times q^b \times \rho^c \quad (9)$$

The unit of π_1 is:

$$[\pi_1] = \left[\frac{L^2}{T} \right] \times [L]^a \times \left[\frac{L^3}{T} \right]^b \times \left[\frac{M}{L^3} \right]^c \quad (10)$$

Since π_1 is dimensionless, we have:

$$\pi_1 = \frac{\nu \cdot l}{q}, \quad (11)$$

which is similar to the Reynolds number, if l is the characteristic length of the flow channel.

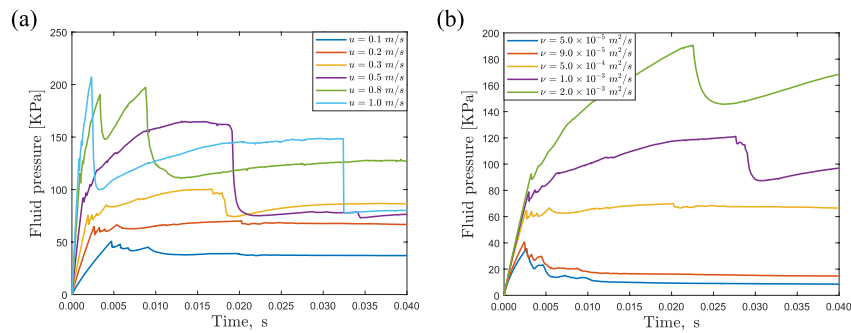


Figure 2. The pore pressure evolution at the record point for cases with different injection rates and fluid viscosity values.

- The second dimensionless parameter π_2 :

$$\pi_2 = S \times l^a \times q^b \times \rho^c \quad (12)$$

The unit of π_2 is:

$$[\pi_2] = \left[\frac{M}{T^2 L} \right] \times [L]^a \times \left[\frac{L^3}{T} \right]^b \times \left[\frac{M}{L^3} \right]^c \quad (13)$$

Since π_2 is dimensionless, we have:

$$\pi_2 = \frac{S l^4}{q^2 \rho} = \frac{S}{\rho q^2 / l^4}, \quad (14)$$

where the denominator part is equivalent to the dynamic pressure term $\frac{1}{2} \rho u^2$.

To estimate proper injection rates and stress levels, we take the experiment parameters from Liu et al. (2018), that is, $q = 3.26 \times 10^{-7} \text{ m}^3/\text{s}$, $\nu = 6.7 \times 10^{-5} \text{ m}^2/\text{s}$, $S = 5.7 \times 10^6 \text{ Pa}$, and $\rho = 1,000 \text{ kg}/\text{m}^3$. The particle size l is estimated as $5.0 \times 10^{-3} \text{ m}$ for the glutenite rock used in the experiment. On the simulation side, we choose the dynamic viscosity as $\nu_s = 5.0 \times 10^{-4} \text{ m}^2/\text{s}$ and fluid density as $\rho_s = 1,000 \text{ kg}/\text{m}^3$. The particle size is estimated by $l_s = 0.25 \sqrt{A_{\max}}$, where $A_{\max} = 5.0 \times 10^{-6} \text{ m}^2$ is the maximum particle area in the simulation. Correspondingly, the injection rate in the simulation is estimated from π_1 , $q_s = 2.72 \times 10^{-7} \text{ m}^3/\text{s}$, and the corresponding injection velocity is $u_s = 0.34 \text{ m}/\text{s}$. From π_2 , the proper magnitude of tensile strength can be estimated. Please note that the tensile strength in the simulation should be scaled according to the elastic modulus and failure criterion. As a result, a stress magnitude of 10 MPa in the experiment corresponds to $1.68 \times 10^4 \text{ Pa}$ in the simulation. In this way, proper values of injection rates and stress levels are found for the simulation with an appropriate magnitude.

3. Results

We systematically investigated the impacts of various factors, including treatment parameters, formation parameters, and rock properties. To ensure strict control over these factors, reference values are established for each parameter as follows: 0.2 m/s for the injection velocity, $5.0 \times 10^{-4} \text{ m}^2/\text{s}$ for the fluid kinematic viscosity, no stress state, the absence of natural fractures, homogeneous bond strengths and a solid volume fraction of 0.97 for the formation permeability.

3.1. Impact of Treatment Parameters

In this section, two major treatment parameters, injection rates and fluid viscosity, are analyzed. Six different injection velocities and fluid viscosity values are chosen for the investigation with the other parameters fixed at the reference value.

The pore pressure variations of the inlet position (the record point shown in Figure 1a) are shown in Figure 2. With injection velocity and viscosity increases, the fracture initiation pressure also increases. The results are consistent with observations from lab experiments and numerical simulation (Duan et al., 2018; Morgan et al., 2017;

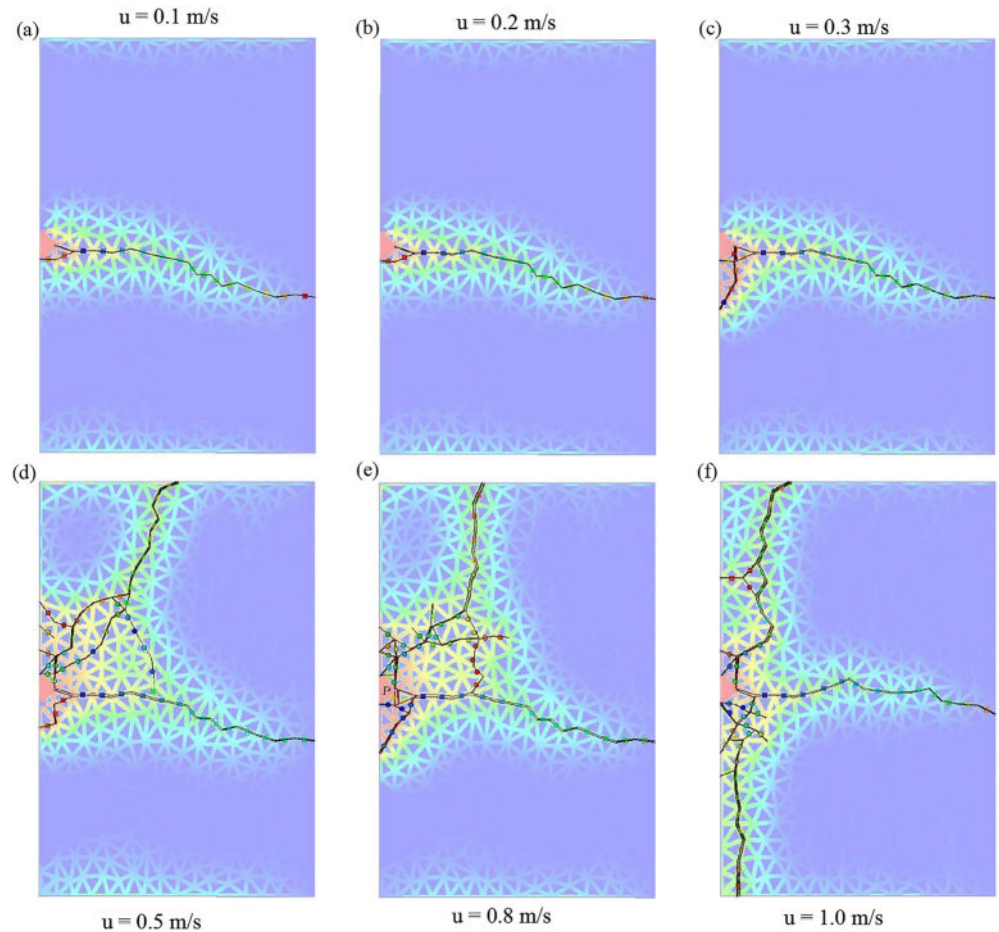


Figure 3. Fracture geometries of cases with different injection rates at 0.04 s. The background shows the fluid pressure distribution in the entire domain. The center of each fracture segment is marked with squares for tensile fractures and circles for shear fractures. The color variations from blue to red refer to the generation sequence of each type of fractures.

Zhuang et al., 2019). However, the mechanism behind the increase in two cases are different. For low injection velocities ($u = 0.1$ and 0.2 m/s), the pore pressure vibrates, but decreases with fracture propagation, which indicates that the fracture volume and leak-off volume expand at a roughly equal or a slightly greater rate than the injection rate. For high injection velocities ($u > 0.2$ m/s), the pore pressure continues to increase after the fracture initiation, indicating that the fracture volume and leak-off volume increase at a smaller rate than the injection rate. In the case of viscosity, a more viscous fluid results in increased viscous resistance, which subsequently requires higher pressure to propel the viscous fluid and fracture the rock.

The fracture geometries of cases with different injection velocities are shown in Figure 3 with the fluid pressure distribution shown in the background. The center point of each fracture is represented by a solid square for a tensile fracture and a circle for a shear fracture. The color variations from cold (blue) to warm (red) refer to the sequence of generation. For low injection velocity, the fracture geometries are almost the same (Figures 3a and 3b). However, with the increasing injection velocities, the fracture geometries become complex with branches. The main horizontal fractures in different cases are similar. However, when the horizontal fracture reaches the right boundary, vertical fractures tend to form at a high injection velocity and most fractures generated in the transition zones (from horizontal to vertical) are shear instead of tensile fractures. When the horizontal fracture reaches the right boundary, the pore pressure in the hydraulic fracture compresses the sample in the top-bottom direction. The stress condition makes the newly generated fracture perpendicular to the horizontal fracture because the fracture trace should be perpendicular to the minimum principle stress (zero stress in the left-right direction). In addition, when the injection velocity is high, the pore pressure becomes significantly high as shown in Figure 2a, which is large enough to generate new fractures in the top-bottom direction.

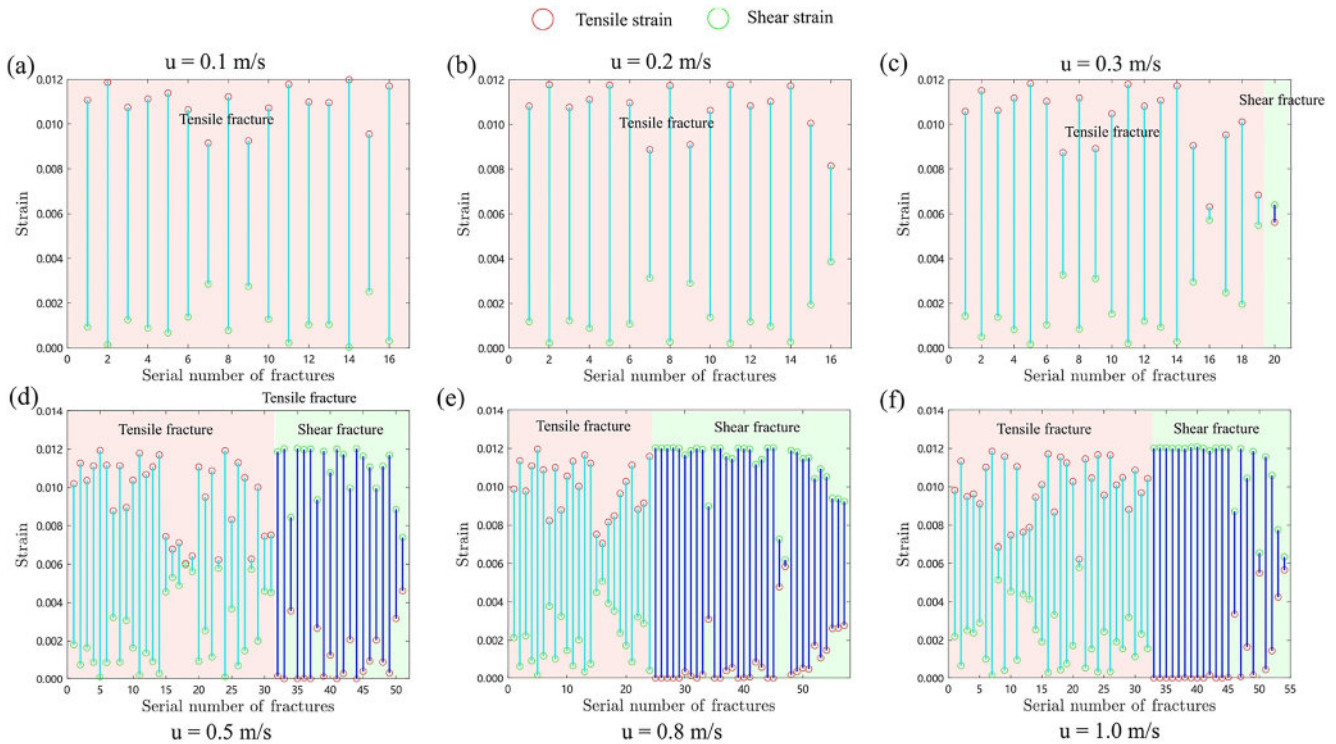


Figure 4. Tensile and shear strain of each fracture segment in Figure 3.

Figure 4 shows the tensile and shear strain component of each fracture segment in Figure 3. The tensile and shear strains are represented with red and green circles, respectively. The links between tensile and shear strain for tensile and shear fractures are light blue and regular blue. When the injection rate is small, all fractures are tensile fractures with insignificant shear strain between particles. However, when the injection rate increases, more fractures have a comparable even larger shear strain than tensile strain. The proportion of shear fractures increases with the increasing injection velocity, which is consistent with the observation in Duan et al. (2018).

For cases with different fluid viscosity, the fracture geometries are similar and three examples are presented in upper panel of Figure 5.

When the viscosity is low, the fluid can leak into the formation easily and make the pore pressure of the formation increase as shown in Figure 5a. Also, few branches along the main hydraulic fracture can be observed in Figure 5a. For high-viscosity fluid, the pore pressure can only propagate to the neighboring region and the region area shrinks with increasing viscosity. In addition, after the horizontal fracture reaches the right boundary, new fractures can be generated at the inlet because of the high pore pressure therein as shown in Figure 2b. The lower panel of Figure 5 presents the strain component of each fracture segment. When the viscosity is low, all generated fractures are tensile fractures. With the increasing viscosity, the shear strain becomes more significant and the proportion of shear fractures also increases. However, the main horizontal fractures are mostly tensile and shear fractures are usually the newly generated inclined fractures.

Fluid with low viscosity has stronger penetration capability than highly viscous fluid. Figure 6 shows the pressure distribution of cases with low and high fluid viscosity at the fracture initiation stage. The pressure propagates much farther in the low-viscosity case. Similar observations are obtained from Duan et al. (2018) and Z. Chen et al. (2020). The penetration capability may not significantly change the fracture geometries in homogeneous media since all bonds are equally strong. However, in heterogeneous media with high injection rates, this penetration capability can help generate more complex fracture geometries (Z. Chen et al., 2020). The impacts of multiple factors will be discussed in the following section.

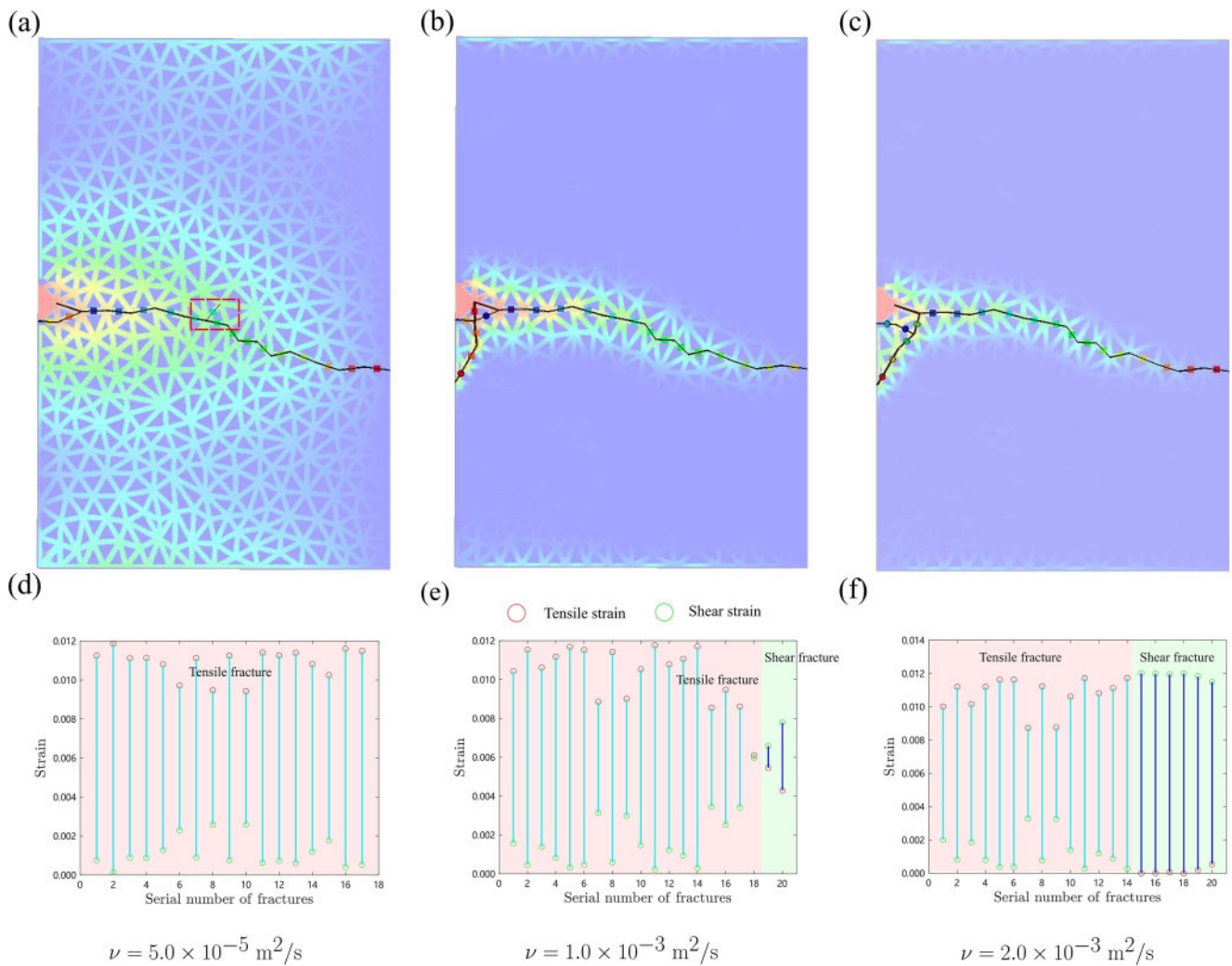


Figure 5. Upper panel: fracture geometries of cases with different fluid viscosity at 0.04 s. A branch generated in the low-viscosity case is marked in the red box. Lower panel: tensile and shear strain of each fracture segment in the upper panel.

3.2. Impact of Formation Parameters

In this section, we investigate the individual impact of in situ stress states and the existence of natural fractures. The stress in the top-bottom direction is fixed at 1.68×10^4 Pa, as derived in Section 2. Different stress anisotropy degrees are represented by the stress ratio between σ_{lr} (left-right direction) and σ_{tb} (top-bottom direction). Six levels of the ratio are chosen for the investigation: $\sigma_{lr}/\sigma_{tb} = 1.0, 1.3, 1.5, 1.7, 1.9, 0$.

The pore pressure variations of each case at the record point are shown in Figure 7, where the initiation pressure increases due to the imposed in situ stresses. A larger imposed in situ stress leads to a higher fracture initiation pressure.

However, the implementation of in situ stress does not change the fracture geometry significantly. For the first five cases, where σ_{lr} is the maximum principle stress, the fracture geometries are similar and have a direction perpendicular to the minimum stress direction (top-bottom direction). Two examples with $\sigma_{lr}/\sigma_{tb} = 1.0$ and 1.9 are shown in Figures 8a and 8b. For the case where no stress applies in the left-right direction, the fracture propagates in the top-bottom direction as expected, which is perpendicular to the minimum principle stress.

The lower panel of Figure 8 shows the tensile and shear strain of each generated fracture in the upper panel. The fractures are dominated by tensile fractures, but the shear fractures tend to increase with the anisotropy level. In

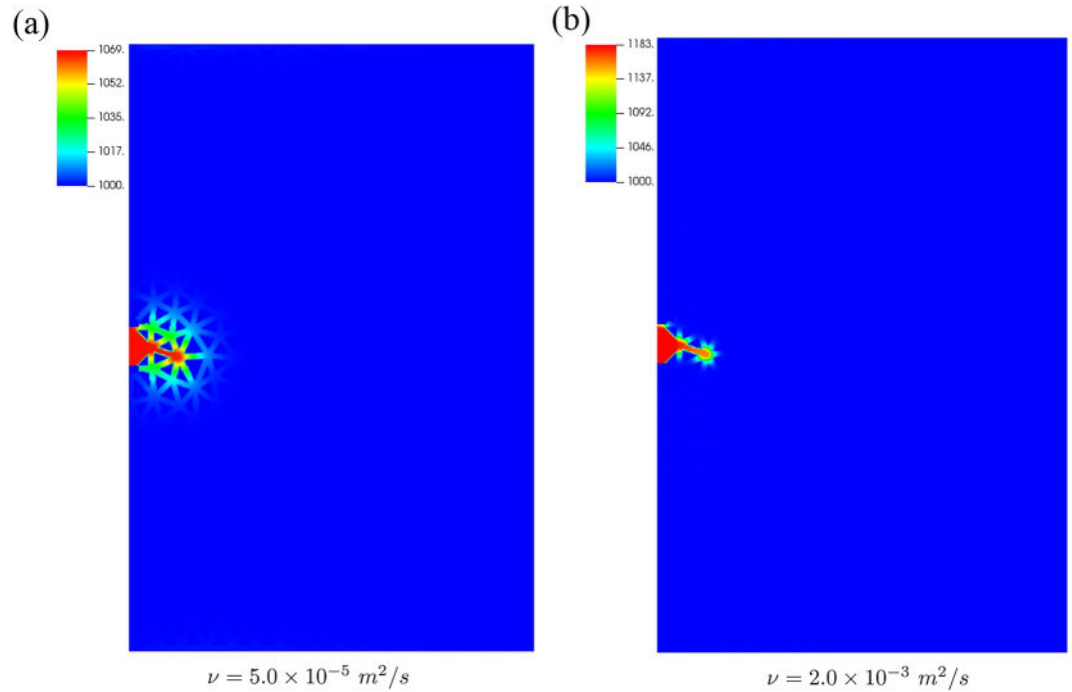


Figure 6. Fluid density distribution at the fracture initiation stage for cases with a low (a) and high (b) fluid viscosity, respectively. The corresponding pore pressure can be converted using Equation 4.

addition, compared with the cases with no stress imposed (Figure 4a), several tensile fractures have more significant shear strain components.

Natural fractures are ubiquitous in the subsurface, and always form complex fracture networks. They play an vital role in the creation of complex fracture networks in the hydraulic fracturing process, also known as SRV. However, natural fractures have complex distributions, including fracture lengths, positions, and orientations, as well as interactions between them and relative strengths compared to the rock matrix. In this work, we demonstrate the capability of the DEM-LBM scheme to simulate natural fractures and investigate their impact. A more extensive investigation to study natural fractures will be presented in separate future research.

Natural fractures are simulated by modifying the strengths of bonds. Only one natural fracture is inserted in the calculation domain (gray bonds in Figure 9), while more natural fractures can be introduced without difficulties in a larger domain. Here, results with $\epsilon_f = 0.33\epsilon_{th}$ and $\epsilon_f = 0.67\epsilon_{th}$ are presented, where ϵ_f denotes the bond strength of natural fractures. The fracture networks generated are shown in Figure 9.

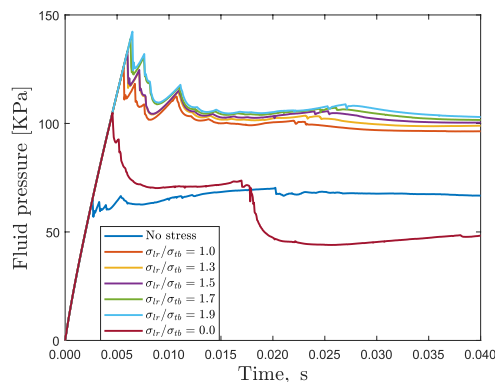


Figure 7. The pore pressure evolution at the record point for cases with different in situ stress states.

When the bond strengths are small, the hydraulic fracture will propagate along the natural fracture upon encountering it. Natural fractures generally undergo shear failure under the given in situ stress states, where the longitudinal stress (σ_{lr}) is greater than the transverse stress (σ_{tb}). Subsequently, the hydraulic fracture will continue to grow in the initial orientation. When the fracture strength is large, the hydraulic fracture will cross the natural fracture and continue to grow in the original orientation. The horizontal fractures are primarily dominated by tensile fractures, while the inclined fracture branches are dominated by shear fractures. In general, the presence of natural fractures can significantly alter the complexity of the fracture network. Further in-depth research will be conducted in future work.

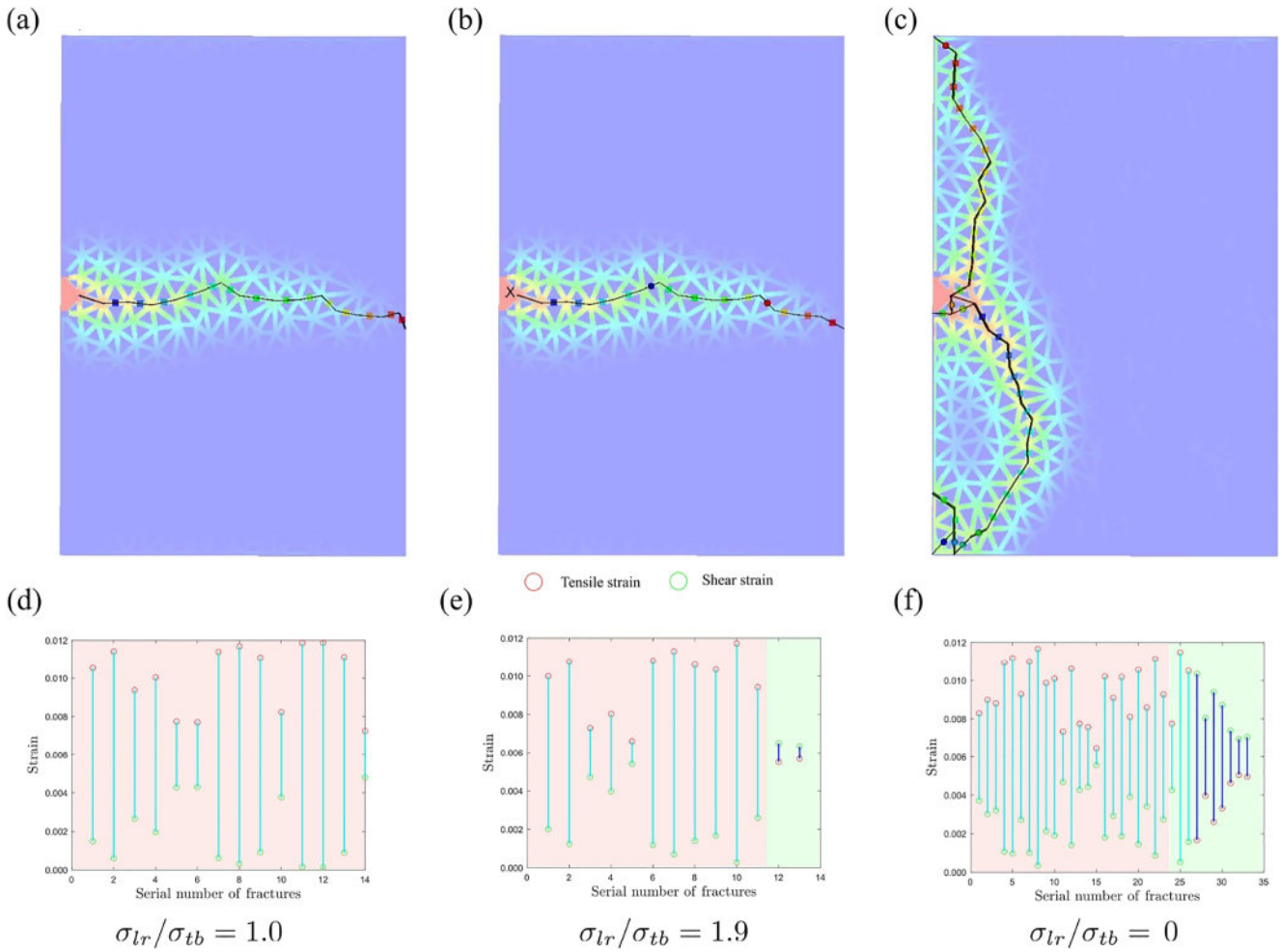


Figure 8. Upper panel: fracture geometries of cases with different in situ stress states at 0.04 s; Lower panel: tensile and shear strain of each fracture segment in the upper panel.

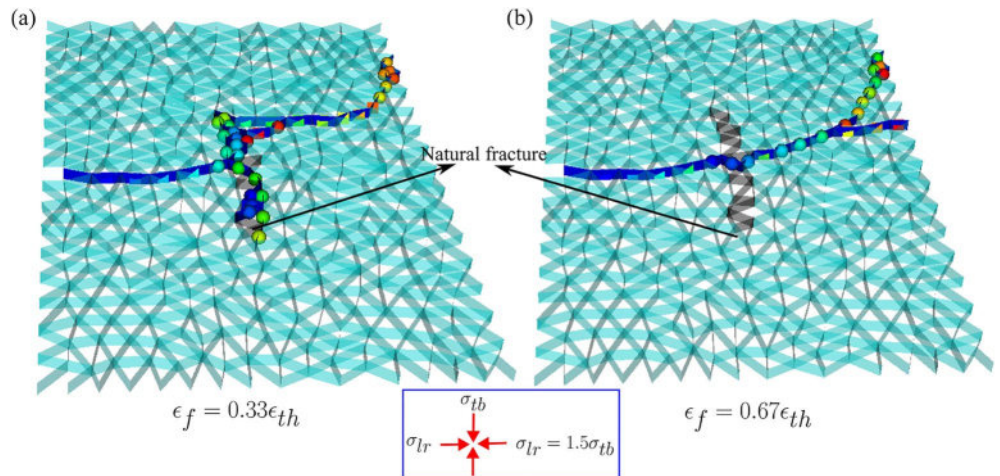


Figure 9. The fracture geometries of cases with the existence of one natural fracture.

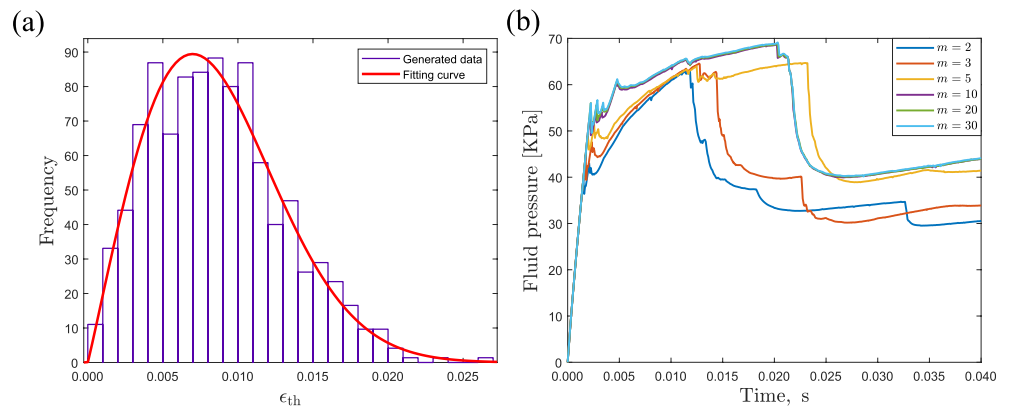


Figure 10. (a) A Weibull distribution fitting of heterogeneous bond strengths (b) The pore pressure evolution at the record point for cases with different heterogeneity degrees of bond strengths.

3.3. Impact of Rock Properties

In this section, we investigate two intrinsic rock properties, heterogeneity of bond strengths and rock permeability. To investigate the heterogeneous characteristic of natural rocks, we choose different values of m in the Weibull distribution to make the bond strength vary. The average bond strength is 0.01 and six values of m are chosen for the consideration: $m = 2, 3, 5, 10, 20, 30$. A smaller m value represents a higher heterogeneity degree. For the case with $m = 2$, the strength distribution and the fitting curve are shown in Figure 10a. The fitting parameters are 0.0097 for the mean and 2.04 for the shape factor, m . Therefore, the chosen quantity of particles (741) is sufficient to recover the prescribed distribution for the heterogeneous bond strengths. Permeability controls the seepage capability of rocks. In this work, the rock permeability is controlled by the solid volume fraction (γ) in the IBM, which has a negative correlation with the formation permeability. A larger γ indicates that more voids are occupied by impermeable solids and the corresponding formation permeability is lower. Impacts of different values of solid volume fractions (γ) are evaluated and six values are chosen: $\gamma = 0.85, 0.9, 0.92, 0.95, 0.97, 0.99$.

For different heterogeneity degrees, the pore pressure variations of each case at the record point are shown in Figure 10b. The pressure buildup process is the same for all cases with different heterogeneity. The initiation pressure is higher for cases with more homogeneous levels. The most heterogeneous case, where $m = 2.0$, has the lowest initiation pressure. However, the pore pressure continues to increase during the propagation of fractures and the increase is more significant for heterogeneous cases.

The fracture geometries of each case are shown in Figure 11.

The higher the heterogeneity degree is, the more complex the fracture geometry is. For the case with $m = 2.0$, the fracture geometries are the most complex with several branches. There are also some fractures disconnected from the main fractures, which can be attributed to two main reasons: one is the leakage of fluid into the matrix, second one is the imposed compressive stress caused by increased pore pressure in the main fractures. To better demonstrate this process, the fracture traces are plotted with the bond strength and generation sequence marked in Figure 12. Most disconnected fractures are shear fractures and their bond strengths are quite low as shown in Figure 12b. For the disconnected fractures, the leakage of injected fluid can enhance the pore pressure therein and the high pressure in the main hydraulic fracture can increase the local principal stresses. The increased principal stresses usually stifle possible microseismicity from occurring as concluded in Warpinski et al. (2001). However, there are no initial stresses applied in this simulation, therefore, the increase of principle stresses and pore pressure can cause the shear failure or even tensile failure of those weak bonds.

For more homogeneous cases, where m is large, the fracture geometries do not change significantly. However, compared with a completely homogeneous case (Figure 3a), there are two branches of fractures instead of a single horizontal one, which is similar to the experiment results in Liu et al. (2018).

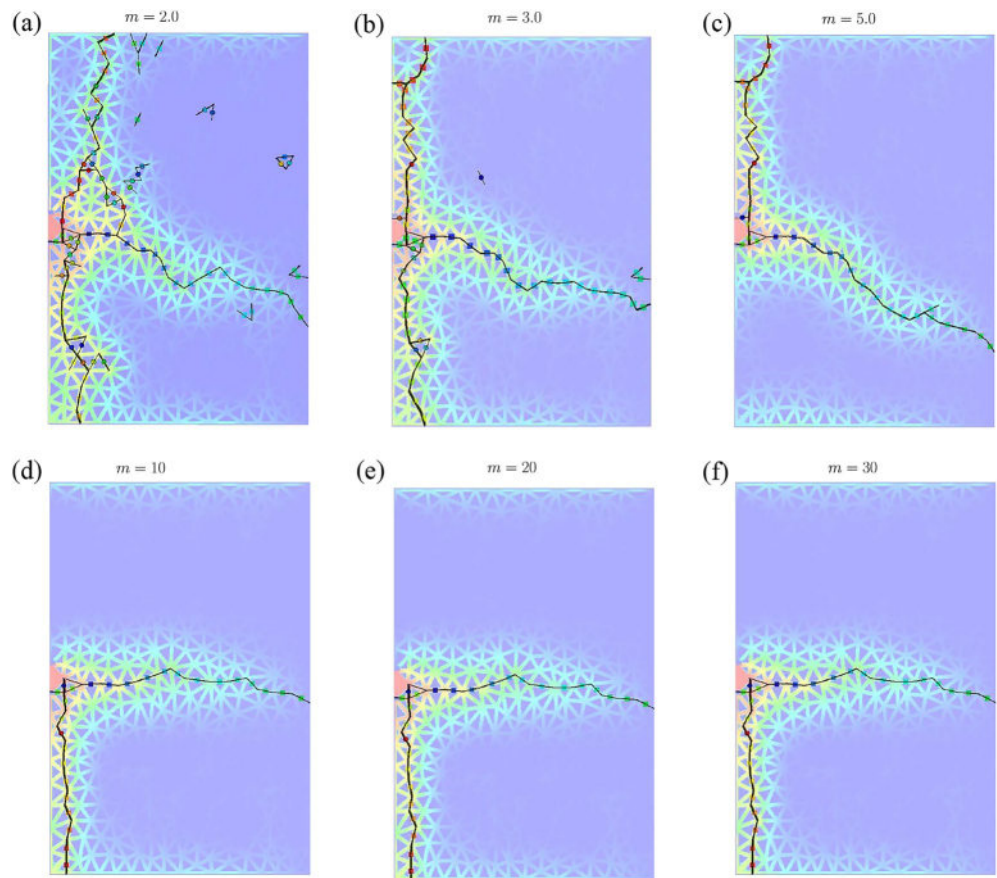


Figure 11. Fracture geometries of cases with different heterogeneity degrees of bond strengths at 0.04 s.

The strain components of each fracture in Figure 11 are shown in Figure 13. For highly heterogeneous cases, many shear fractures are generated. For the most heterogeneous case, 32 out of 78 fractures are shear fractures, corresponding to a proportion of 41%. With the heterogeneity degree decreases, the proportion of shear fractures decreases sharply and tensile fractures are dominated.

For cases with different rock permeability values, the pore pressure variations at the record point for different cases are shown in Figure 14.

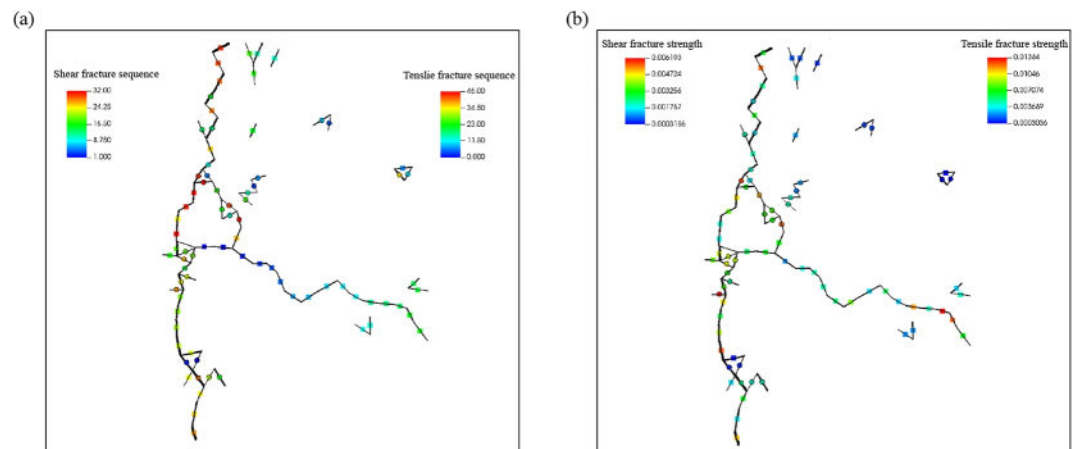


Figure 12. The generation sequence (a) and bond strength (b) of each fracture segment.

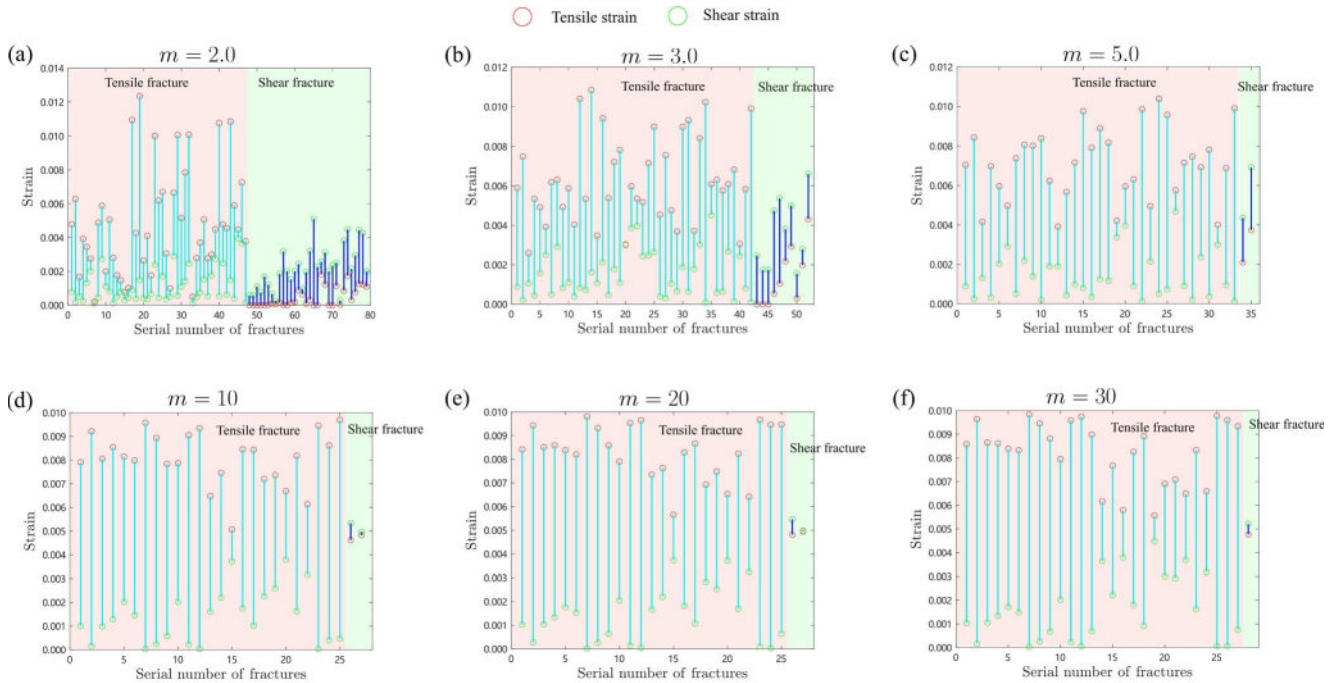


Figure 13. Tensile and shear strain of each fracture segment in Figure 11.

The pressure evolution curves have similar shapes. The lower the matrix permeability, the higher the fracture initiation pressure is, which is consistent with the observations in the lab experiments (Fazio et al., 2021). The fracture geometries are similar for all cases, which are horizontal. Three examples with $\gamma = 0.85$, 0.92, and 0.99 are shown in Figure 15. All generated fractures are tensile fractures with insignificant shear strain.

The matrix permeability controls the leakage of fluid as shown in Figure 15 at a initiation stage. The pressure propagates to a larger region in a highly permeable case (Figure 15a) and the influential region is quite narrow for the weakly permeable case (Figure 15c). To better demonstrate this phenomenon, the pressure distributions at the fracture initiation of the case with $\gamma = 0.85$ and $\gamma = 0.99$ are shown in Figure 16. For the case with $\gamma = 0.99$, the pore pressure is quite high in the cave and the preset fracture but hardly propagates to the neighboring region. For the case with $\gamma = 0.85$, the pressure propagates to a much larger region.

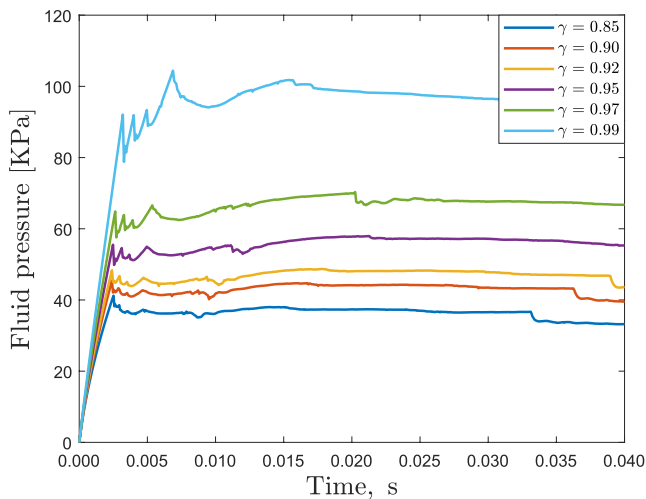


Figure 14. The pore pressure evolution at the record point for cases with different matrix permeability.

3.4. Impacts of Multiple Factors

Based on the analysis of individual factors, it is evident that the complexity of generated fractures is significantly influenced by the injection rate and the degree of heterogeneity, as opposed to fluid viscosity, in situ stress, and rock permeability. Low fluid viscosity and high rock permeability facilitate the propagation of fluid pressure to deeper formations, but these factors have minimal impact on the generation of complex fracture networks in homogeneous rocks. Rock permeability and heterogeneous bond strengths are the intrinsic rock properties, but injection rates and viscosity of fluid are adjustable treatment parameters. Low viscosity fluid, also referred to as slickwater, is usually used as the fracturing fluid (Barati & Liang, 2014) to have a better performance. Therefore, this section focuses on examining the influence of low viscosity fluid in low permeability heterogeneous formations with different injection rates.

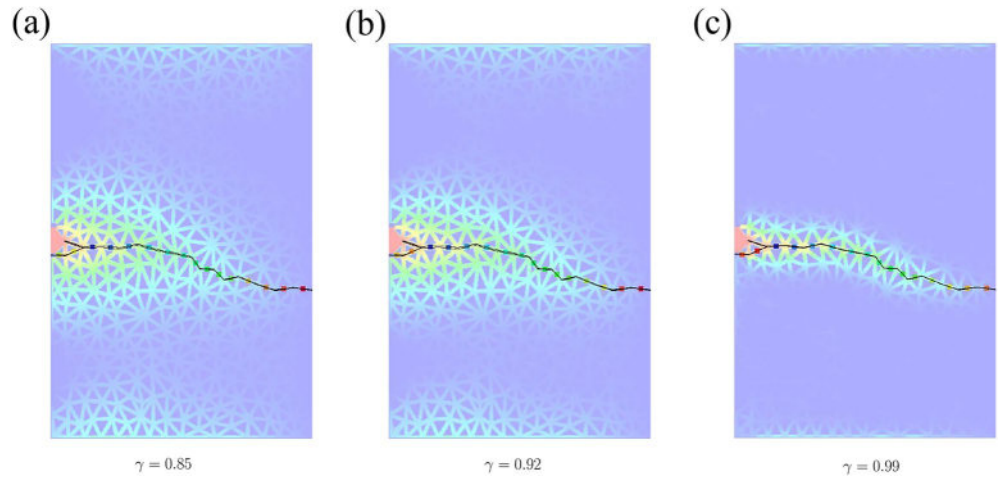


Figure 15. Fracture geometries of cases with different formation permeability at 0.04 s.

We set $\gamma = 0.97$ to represent a low-permeability formation, and $m = 2$ to simulate a heterogeneous media. Without considering the in situ stress, the generated fracture networks are shown in Figure 17b, where tensile fractures dominate, consistent with the findings of Z. Chen et al. (2020). Additionally, a few bonds with low strengths, which are disconnected from the primary hydraulic fracture, can also break either in tensile or shear form due to fluid leakoff and changes in in situ stress caused by the injected fluid.

As the overburden rocks increase, the geostresses become more significant with increasing depth. To mimic the in situ stress in the subsurface, we set $\sigma_{lr} = 1.5\sigma_{lb}$. In situ stress typically hinders the generation of hydraulic fracturing since the pore pressure needs to overcome the minimum principal stress and cohesive strengths of particle bonds. When the degree of heterogeneity is high (e.g., $m = 2$), we observe that many extremely weak bonds break in shear (with a few breaking in tension) even without the injection of fluid. However, in a stable subsurface formation, such a phenomenon is unlikely because extremely weak broken bonds can be healed over a long geological time through mineral growth. Therefore, we set $m = 4.2$ to introduce heterogeneity in bond strengths

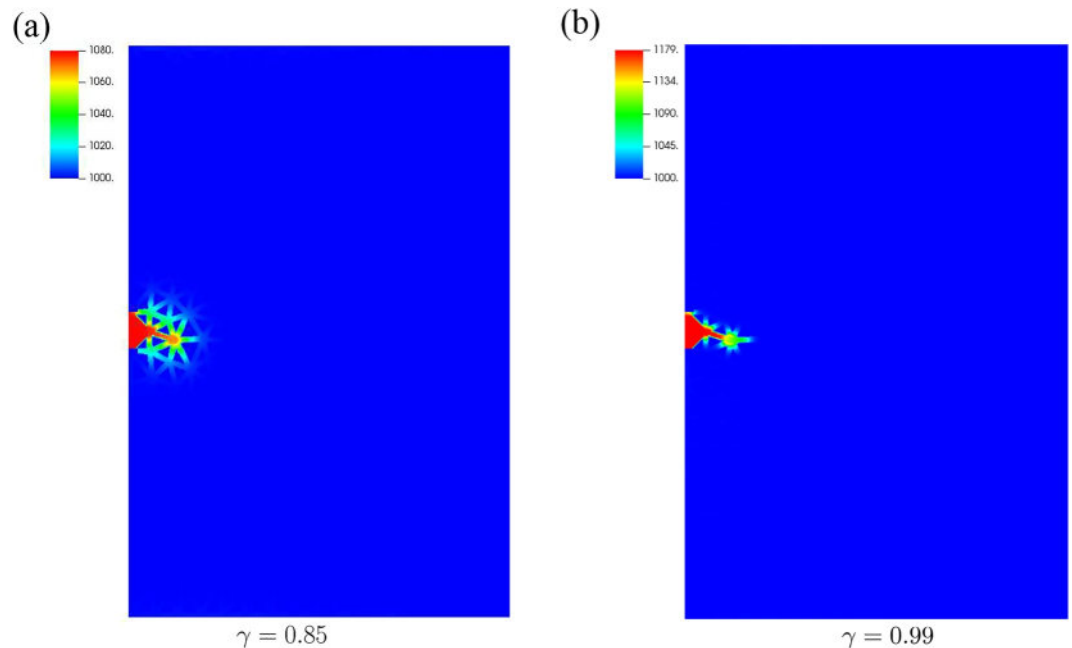


Figure 16. Fluid density distribution at the fracture initiation stage for cases with a high (a) and low (b) formation permeability, respectively. The corresponding pore pressure can be converted using Equation 4.

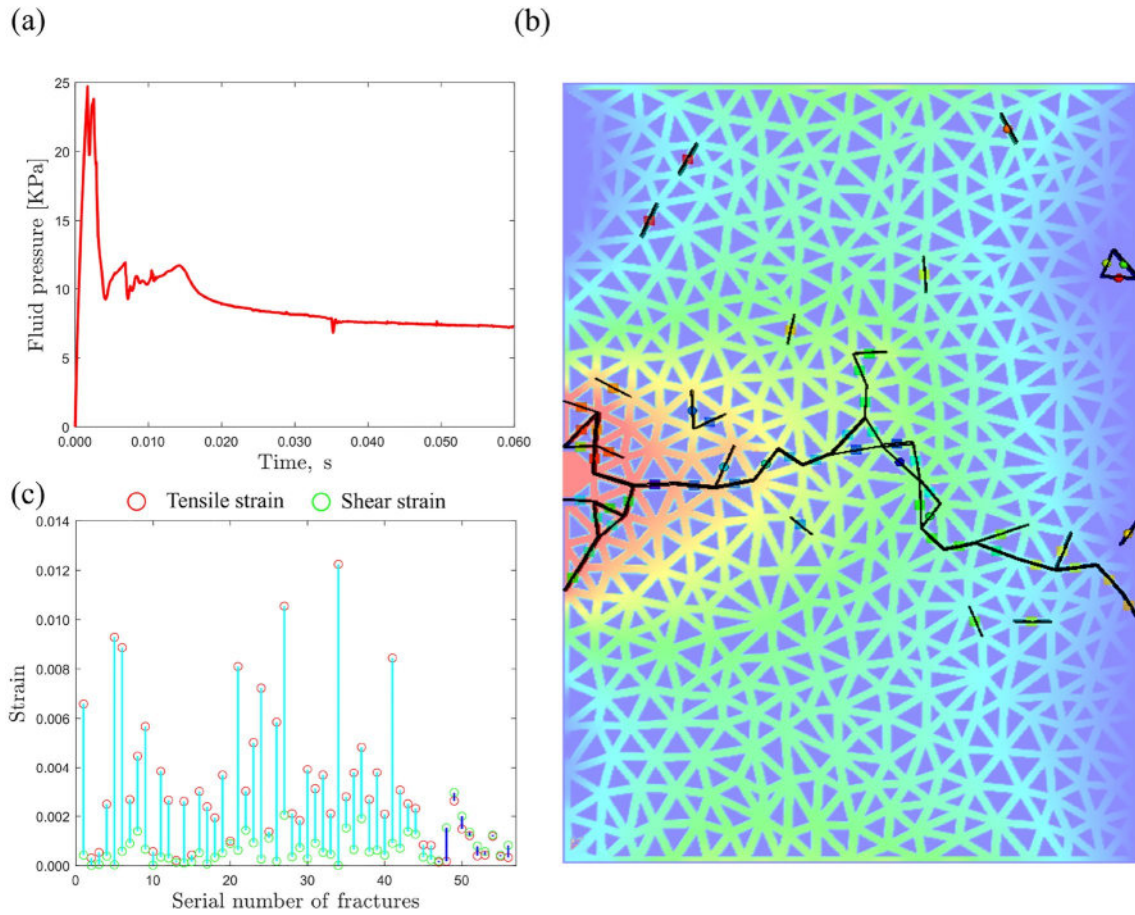


Figure 17. (a) The pore pressure evolution at the recorded point for the low-viscosity fluid with no in situ stress applied (b) Fracture geometries at 0.06 s (c) Tensile and shear strain of each fracture segment in (b).

while simultaneously ensuring that no bonds are broken under the given in situ stress. Under this condition, we further investigate the impact of low-viscosity fluid on the generation of complex fracture networks. We apply a low injection rate of 0.2 m/s and a high injection rate of 0.5 m/s.

For the case with a low injection rate, the evolution of injected pore pressure is shown in Figure 18a, and the generated fracture network is shown in Figure 18b. The primary hydraulic fracture stops growing when it encounters bonds with high strengths. It is difficult for the low-viscosity fluid to build up significant pressure due to substantial leakoff into the matrix. Several shear fractures are formed and disconnected from the primary hydraulic fracture. These shear fractures are typically weak bonds that break due to the disturbed in situ stress caused by the injected fluid.

In order to enhance the injected pressure and strengthen the proppant transport capability, a high injection rate is usually adopted in real applications (Barati & Liang, 2014). As observed, with a high injection velocity, the pressure buildup is more significant, as shown in Figure 19a. The corresponding fracture network becomes much more complex, as shown in Figure 19b. These complex fracture networks are mainly composed of shear fractures rather than tensile fractures, as illustrated in Figure 19c. The generation of shear fractures is also attributed to the enhanced pore pressure resulting from leakoff and alterations in in situ stress caused by injection pressure. Moreover, the enhanced pore pressure may play an essential role, as observed in Figure 19b, where the pore pressure can be conveniently transported to the entire domain due to the low-viscosity fluid and broken bonds, leading to further bond breakage and the formation of more complex fracture networks.

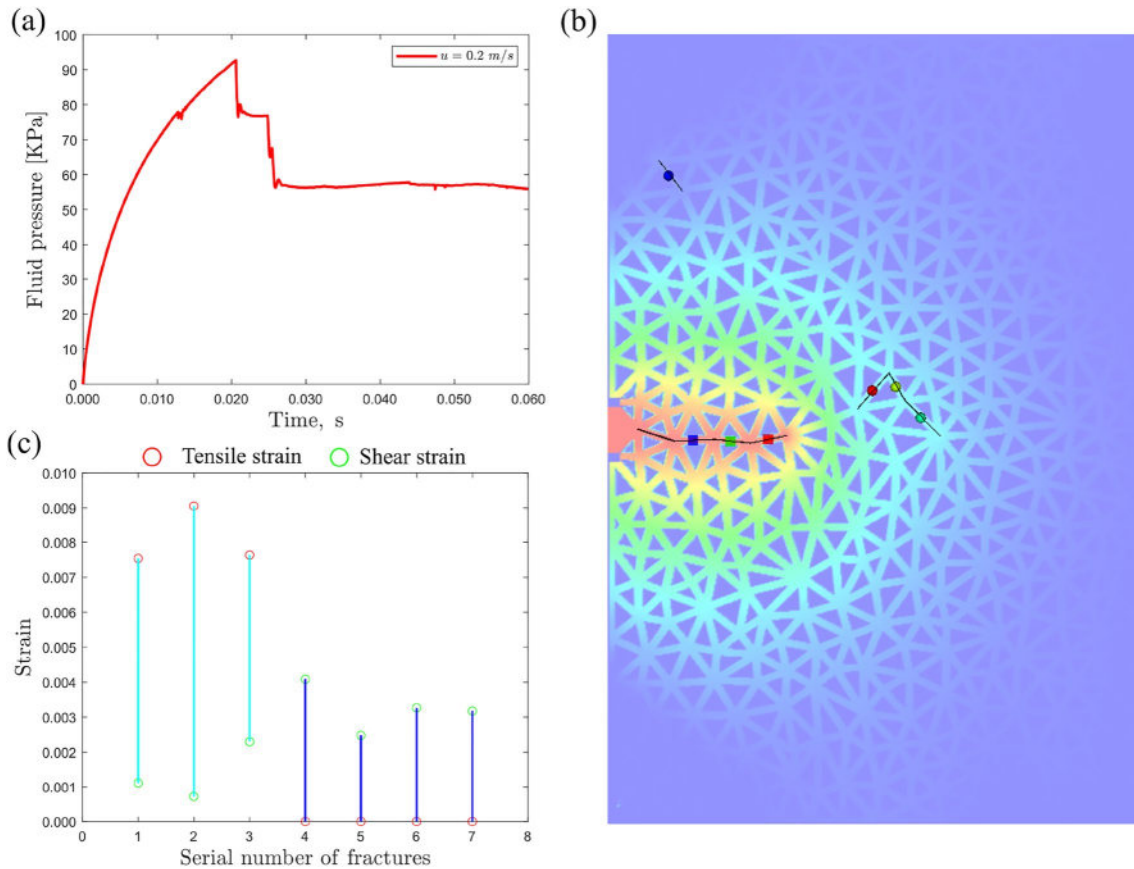


Figure 18. (a) The pore pressure evolution at the recorded point for the low-viscosity fluid with an injection rate of 0.2 m/s (b) Fracture geometries at 0.06 s (c) Tensile and shear strain of each fracture segment in (b).

4. Discussions

In this work, we conducted a systematic analysis of the impacts of different factors, including formation parameters, treatment parameters, and rock properties, on the fracture initiation and propagation process. Each factor was evaluated independently with the other factors fixed, allowing for a comprehensive and detailed understanding of its individual impact. Subsequently, we performed an analysis of multiple factors, focusing on the impact of low-viscosity fluid on hydraulic fracturing in low-permeability heterogeneous formations.

Most primary hydraulic fractures (horizontal ones in most cases) are tensile fractures in the individual factor analysis. However, when the primary fracture reaches the right boundary, vertical tensile fractures are possible if the pore pressure is high enough. In the transition zone, shear fractures are more dominant than tensile fractures, like Figures 3d–3f, Figure 5b, and Figures 11a–11c. The generated shear fractures are usually inclined and a Mohr's circle analysis may explain this phenomenon. In Figure 20, a Mohr's circle and stress states of three planes (blue, green, and red) are determined by the intersection point between the plane and the Mohr's circle. For the demonstration purpose, the friction coefficient is 0.4 and the cohesion strength is set to zero. The specific Mohr's circle in the simulation domain is caused by the enhanced pore pressure from leak-off and principle stresses generated by the compression from the primary hydraulic fracture. The purple arc in Mohr's circle refers to all possible plane directions that can trigger a shear failure. The inclined bonds are more likely to form shear failures because their orientations fall into the shear failure range.

The DEM-LBM coupled method is powerful to investigate the detailed fracture initiation and propagation process. However, there are still several limitations and two important ones are listed below:

- The roughness of the fracture surface is difficult to be reproduced with DEM since there are large differences in scales between the particle size and asperity size. Therefore the shear dilation process is hard to mimic,

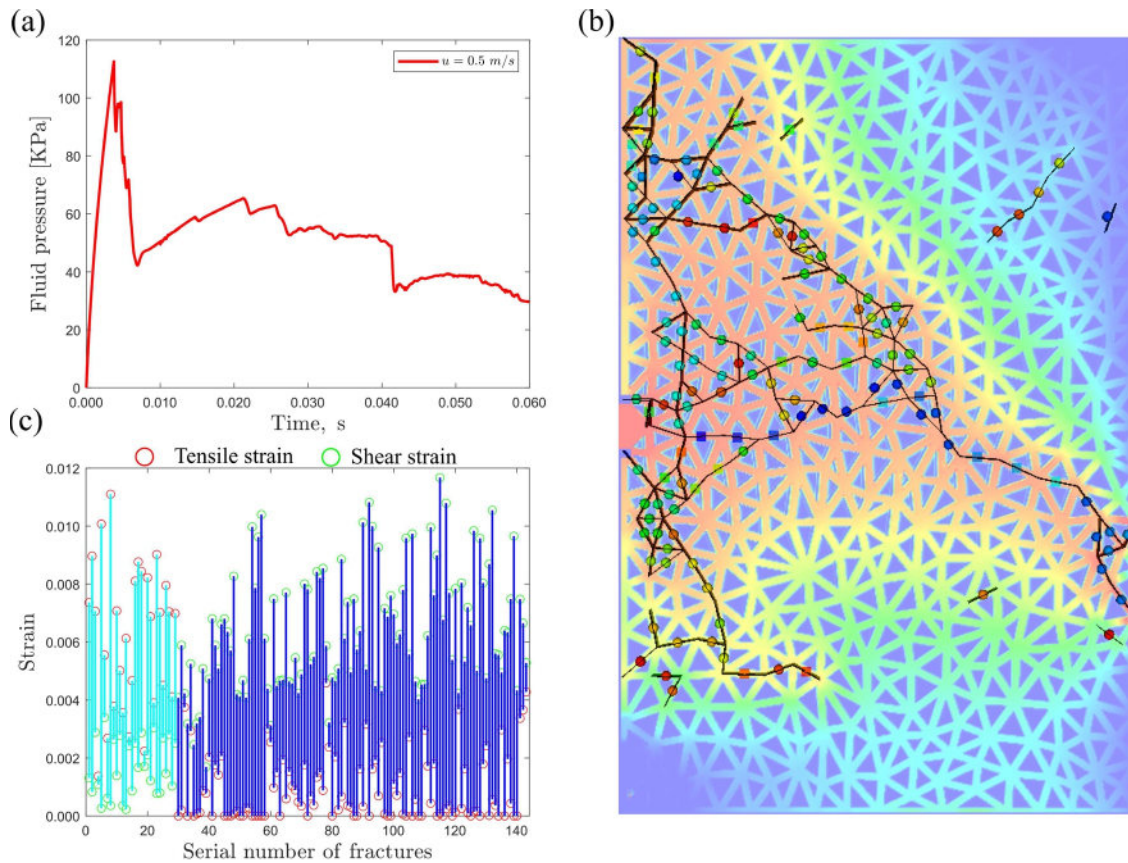


Figure 19. (a) The pore pressure evolution at the recorded point for the low-viscosity fluid with an injection rate of 0.5 m/s (b) Fracture geometries at 0.06 s (c) Tensile and shear strain of each fracture segment in (b).

which is also an important mechanism to form complex fracture networks in a hydraulic fracturing process (Rahman et al., 2002).

- The breakage of particles is not applicable in this DEM scheme. Therefore, only breakage between particles is possible. However, several experiments observed that hydraulic fractures can cut the minerals and propagate across particles, especially in hydraulic fracturing with critical CO₂ (Y. Chen et al., 2015),

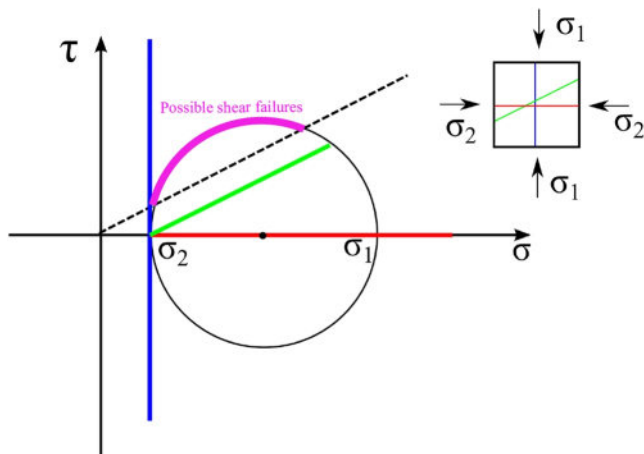


Figure 20. A sketch map of a Mohr's circle for different fracture planes (red, blue, and green).

Therefore, improvements in the numerical scheme or the development of new schemes are still necessary to simulate the hydraulic fracturing process in reality. Furthermore, this work presents a feasible framework to investigate the hydraulic fracturing process with multiple variables, which is essential to understand the mechanism behind the formation of the SRV. Complex natural fracture networks can be incorporated into a much larger domain, which will be the focus of subsequent research in the future.

5. Conclusions

In this work, a comprehensive investigation of the influential factors on the initiation and propagation in a hydraulic fracturing process is conducted with the DEM-LBM method. The factors include treatment parameters (injection rates and fluid viscosity), formation parameters (in situ stress states and existence of natural fractures), and rock properties (heterogeneity of rock strengths and rock permeability). Several important findings and conclusions are drawn below:

- A higher injection rate, increased viscosity, and larger in situ stress will lead to an increase in the initiation pressure. Conversely, higher formation permeability and a greater degree of heterogeneity in bond strengths will result in a decrease in the initiation pressure.
- The complexity of generated fractures is significantly influenced by the injection rate and degree of heterogeneity. However, fluid viscosity, in situ stress states, and formation permeability individually do not affect the geometrical complexity.
- Shear displacement can occur during a hydraulic fracturing process due to increased pore pressure and variations in in situ stress caused by injected fluid. The extent of shear displacement can be significant under specific conditions, including a high injection rate and high degrees of heterogeneity.
- Natural fractures can significantly impact the complexity of generated fracture networks, while more in-depth research is required regarding complex fracture distributions, relative fracture strengths, etc.
- Low-viscosity fluid with a high injection rate can have a significant pressure buildup and generate complex fracture networks in low-permeability heterogeneous formations.

Appendix A: Benchmark Case for LBM Simulation

The Poiseuille flow in a slit driven by gravity is chosen as the benchmark case to validate the LBM algorithm. The slit has lengths and widths of 100 and 48 lattice units (lu). A bounce-back boundary condition is implemented on the top and bottom walls. A periodic boundary condition is adopted to avoid the entry or exit effect for the left and right boundaries.

The Reynolds number is 20 to ensure a laminar flow state. The maximum velocity (u_{\max}) is chosen as 0.1 lu ts^{-1} . The relaxation time (τ) is 1.0 for the simple bounce-back boundaries, which yield a kinematic viscosity (ν) of $1/6 \text{ lu}^2 \text{ ts}^{-1}$. Fluid density (ρ) is chosen as 1.0. The analytical solution for the gravity-driven Poiseuille flow yields a parabolic velocity profile:

$$u(x) = \frac{\rho g}{2\mu}(a^2 - x^2), \quad (\text{A1})$$

where $u(x)$ is the velocity in the Y direction, a is the half width of the slit, g is the gravitational acceleration. The maximum velocity is:

$$u_{\max} = \frac{\rho g a^2}{2\mu} \quad (\text{A2})$$

Through rearranging Equation A2, the corresponding gravitational acceleration (g) to drive the flow is calculated:

$$g = \frac{2\nu u_{\max}}{a^2} \quad (\text{A3})$$

Therefore, g is $5.7804 \times 10^{-5} \text{ lu ts}^{-2}$.

The velocity distribution in the slit is shown in Figures A1a and A1b shows the comparison between the analytical solution and the simulation result.

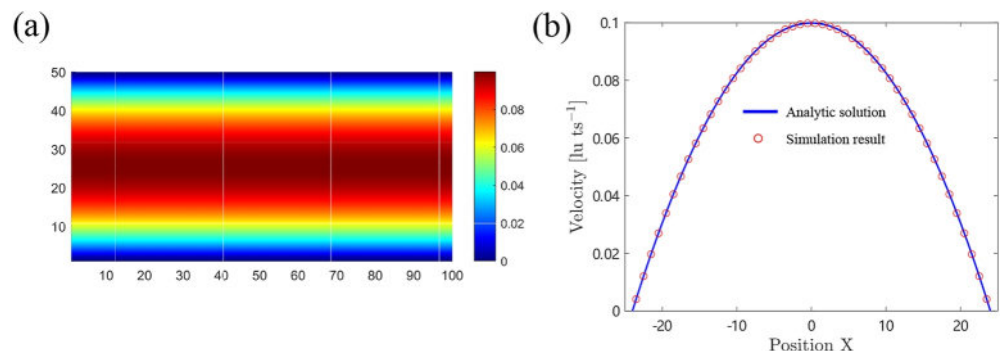


Figure A1. (a) The velocity distribution in a slit (b) Comparison between the analytical solution and lattice Boltzmann method result.

Appendix B: Benchmark Case for the DEM Simulation

A Brazilian test is used to validate the correctness of the DEM simulation. A round disc with a diameter of 0.2 m and a thickness of 0.1 m is generated for the simulation. The total number of particles is 1,924. The specific rock properties are not used in the simulation considering the computational cost. The normal and tangential contact stiffness are 1.0×10^5 N/m. The normal and tangential elastic modulus are 1.0×10^5 Pa. The threshold value on the total strain is 0.02. The time step is chosen as 4.5×10^{-5} s. The breaking results after the compression are shown in Figure B1. A vertical fracture and V-shaped damage zones are observed, and similar results are found in lab experiments (Gong et al., 2019).

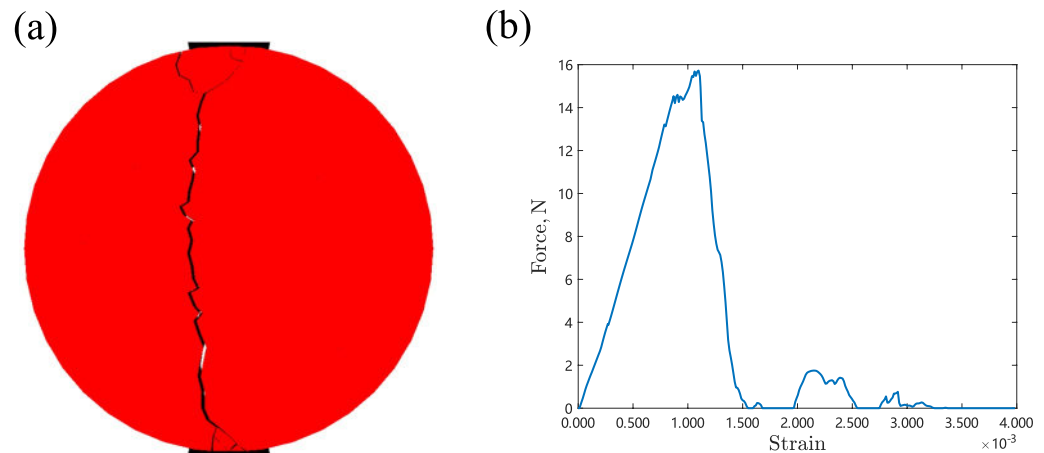


Figure B1. (a) Fractures formed after compression in a Brazilian test (b) The force-strain relation of the Brazilian test.

Data Availability Statement

The numerical simulation in this work is based on the open-source multi-physics simulation library MECHSYS developed by Galindo-Torres (2013b). The library is available at <https://mechsys.nongnu.org/>.

Acknowledgments

This project was supported by the National Key Research and Development Program of China (No. 2019YFA0708704). The numerical simulation is supported by the High Performance Computing Center at Tsinghua University. Furthermore, the authors would like to thank all the editors and anonymous reviewers for their valuable comments and suggestions.

References

- Barati, R., & Liang, J.-T. (2014). A review of fracturing fluid systems used for hydraulic fracturing of oil and gas wells. *Journal of Applied Polymer Science*, 131(16). <https://doi.org/10.1002/app.40735>
- Buckingham, E. (1915). The principle of similitude. *Nature*, 96(2406), 396–397. <https://doi.org/10.1038/096396d0>
- Chen, S., & Doolen, G. D. (1998). Lattice Boltzmann method for fluid flows. *Annual Review of Fluid Mechanics*, 30(1), 329–364. <https://doi.org/10.1146/annurev.fluid.30.1.329>
- Chen, Y., Nagaya, Y., & Ishida, T. (2015). Observations of fractures induced by hydraulic fracturing in anisotropic granite. *Rock Mechanics and Rock Engineering*, 48(4), 1455–1461. <https://doi.org/10.1007/s00603-015-0727-9>
- Chen, Z., Elsworth, D., & Wang, M. (2020). Does low-viscosity fracturing fluid always create complex fractures? *Journal of Geophysical Research: Solid Earth*, 125(9), e2020JB020332. <https://doi.org/10.1029/2020jb020332>
- Chen, Z., Jin, X., & Wang, M. (2018). A new thermo-mechanical coupled DEM model with non-spherical grains for thermally induced damage of rocks. *Journal of the Mechanics and Physics of Solids*, 116, 54–69. <https://doi.org/10.1016/j.jmps.2018.03.023>
- Chen, Z., & Wang, M. (2017). Pore-scale modeling of hydromechanical coupled mechanics in hydrofracturing process. *Journal of Geophysical Research: Solid Earth*, 122(5), 3410–3429. <https://doi.org/10.1002/2017jb013989>
- Cheng, S., Zhang, M., Zhang, X., Wu, B., Chen, Z., Lei, Z., & Tan, P. (2022). Numerical study of hydraulic fracturing near a wellbore using dual boundary element method. *International Journal of Solids and Structures*, 239, 111479. <https://doi.org/10.1016/j.ijsolstr.2022.111479>
- Cundall, P. A., & Strack, O. D. (1979). A discrete numerical model for granular assemblies. *Géotechnique*, 29(1), 47–65. <https://doi.org/10.1680/geot.1979.29.1.47>
- Dahi-Taleghani, A., & Olson, J. E. (2011). Numerical modeling of multistranded-hydraulic-fracture propagation: Accounting for the interaction between induced and natural fractures. *SPE Journal*, 16(03), 575–581. <https://doi.org/10.2118/124884-pa>
- De Pater, C., & Beugelsdijk, L. (2005). Experiments and numerical simulation of hydraulic fracturing in naturally fractured rock. In *Alaska rocks 2005, the 40th us symposium on rock mechanics (USRMS)*.
- Duan, K., Kwok, C. Y., Wu, W., & Jing, L. (2018). DEM modeling of hydraulic fracturing in permeable rock: Influence of viscosity, injection rate and in situ states. *Acta Geotechnica*, 13(5), 1187–1202. <https://doi.org/10.1007/s11440-018-0627-8>
- Fazio, M., Ibemesi, P., Benson, P., Bedoya-González, D., & Sauter, M. (2021). The role of rock matrix permeability in controlling hydraulic fracturing in sandstones. *Rock Mechanics and Rock Engineering*, 54(10), 5269–5294. <https://doi.org/10.1007/s00603-021-02580-2>
- Galindo-Torres, S. A. (2013a). A coupled discrete element lattice Boltzmann method for the simulation of fluid–solid interaction with particles of general shapes. *Computer Methods in Applied Mechanics and Engineering*, 265, 107–119. <https://doi.org/10.1016/j.cma.2013.06.004>

- Galindo-Torres, S. A. (2013b). Multi-physics simulation library [Software]. MechSys. Retrieved from <https://mechsys.nongnu.org/>
- Galindo-Torres, S. A., Pedroso, D., Williams, D., & Li, L. (2012). Breaking processes in three-dimensional bonded granular materials with general shapes. *Computer Physics Communications*, 183(2), 266–277. <https://doi.org/10.1016/j.cpc.2011.10.001>
- Gandossi, L., & Von Estorff, U. (2013). An overview of hydraulic fracturing and other formation stimulation technologies for shale gas production. *European Commission Joint Research Centre Reports*, 26347.
- Geertsma, J., & De Klerk, F. (1969). A rapid method of predicting width and extent of hydraulically induced fractures. *Journal of Petroleum Technology*, 21(12), 1571–1581. <https://doi.org/10.2118/2458-pa>
- Gong, F., Zhang, L., & Wang, S. (2019). Loading rate effect of rock material with the direct tensile and three Brazilian disc tests. *Advances in Civil Engineering*, 2019, 1–8. <https://doi.org/10.1155/2019/6260351>
- Goodfellow, S., Nasser, M., Maxwell, S., & Young, R. (2015). Hydraulic fracture energy budget: Insights from the laboratory. *Geophysical Research Letters*, 42(9), 3179–3187. <https://doi.org/10.1002/2015gl063093>
- Heider, Y. (2021). A review on phase-field modeling of hydraulic fracturing. *Engineering Fracture Mechanics*, 253, 107881. <https://doi.org/10.1016/j.engfracmech.2021.107881>
- Huang, B., & Liu, J. (2017). Experimental investigation of the effect of bedding planes on hydraulic fracturing under true triaxial stress. *Rock Mechanics and Rock Engineering*, 50(10), 2627–2643. <https://doi.org/10.1007/s00603-017-1261-8>
- Khrstianovic, S., & Zheltov, Y. P. (1955). Formation of vertical fractures by means of highly viscous liquid. In *World petroleum congress proceedings* (pp. 579–586).
- Knight, E. E., Rougier, E., Lei, Z., Euser, B., Chau, V., Boyce, S. H., et al. (2020). Hoss: An implementation of the combined finite-discrete element method. *Computational Particle Mechanics*, 7(5), 765–787. <https://doi.org/10.1007/s40571-020-00349-y>
- Kumari, W., Ranjith, P., Perera, M., Li, X., Li, L., Chen, B., et al. (2018). Hydraulic fracturing under high temperature and pressure conditions with micro CT applications: Geothermal energy from hot dry rocks. *Fuel*, 230, 138–154. <https://doi.org/10.1016/j.fuel.2018.05.040>
- Lecampion, B. (2009). An extended finite element method for hydraulic fracture problems. *Communications in Numerical Methods in Engineering*, 25(2), 121–133. <https://doi.org/10.1002/cnm.1111>
- Lei, Z., Rougier, E., Munjiza, A., Viswanathan, H., & Knight, E. E. (2019). Simulation of discrete cracks driven by nearly incompressible fluid via 2D combined finite-discrete element method. *International Journal for Numerical and Analytical Methods in Geomechanics*, 43(9), 1724–1743. <https://doi.org/10.1002/nag.2929>
- Liu, P., Ju, Y., Gao, F., Ranjith, P. G., & Zhang, Q. (2018). CT identification and fractal characterization of 3-D propagation and distribution of hydrofracturing cracks in low-permeability heterogeneous rocks. *Journal of Geophysical Research: Solid Earth*, 123(3), 2156–2173. <https://doi.org/10.1002/2017jb015048>
- Liu, P., Ju, Y., Ranjith, P. G., Zheng, Z., Wang, L., & Wanniarachchi, A. (2016). Visual representation and characterization of three-dimensional hydrofracturing cracks within heterogeneous rock through 3D printing and transparent models. *International Journal of Coal Science & Technology*, 3(3), 284–294. <https://doi.org/10.1007/s40789-016-0145-y>
- Marder, M., Chen, C.-H., & Patzek, T. (2015). Simple models of the hydrofracture process. *Physical Review E*, 92(6), 062408. <https://doi.org/10.1103/physreve.92.062408>
- Mohammadnejad, T., & Khoei, A. (2013). An extended finite element method for hydraulic fracture propagation in deformable porous media with the cohesive crack model. *Finite Elements in Analysis and Design*, 73, 77–95. <https://doi.org/10.1016/j.finel.2013.05.005>
- Morgan, S., Li, B., & Einstein, H. (2017). Effect of injection rate on hydraulic fracturing of opalinus clay shale. In *51st us rock mechanics/geomechanics symposium*.
- Munjiza, A., Owen, D., & Bicanic, N. (1995). A combined finite-discrete element method in transient dynamics of fracturing solids. *Engineering Computations*.
- Munjiza, A., Rougier, E., Lei, Z., & Knight, E. E. (2020). FSIS: A novel fluid–solid interaction solver for fracturing and fragmenting solids. *Computational Particle Mechanics*, 7(5), 789–805. <https://doi.org/10.1007/s40571-020-00314-9>
- Noble, D., & Torczynski, J. (1998). A lattice-Boltzmann method for partially saturated computational cells. *International Journal of Modern Physics C*, 9(08), 1189–1201. <https://doi.org/10.1142/s0129183198001084>
- Nordgren, R. (1972). Propagation of a vertical hydraulic fracture. *Society of Petroleum Engineers Journal*, 12(04), 306–314. <https://doi.org/10.2118/3009-pa>
- Olson, J. E., & Taleghani, A. D. (2009). Modeling simultaneous growth of multiple hydraulic fractures and their interaction with natural fractures. In *SPE hydraulic fracturing technology conference*.
- O’Sullivan, C., & Bray, J. D. (2004). Selecting a suitable time step for discrete element simulations that use the central difference time integration scheme. *Engineering Computations*, 21(2/3/4), 278–303. <https://doi.org/10.1108/02644400410519794>
- Peirce, A., & Detournay, E. (2009). An Eulerian moving front algorithm with weak-form tip asymptotics for modeling hydraulically driven fractures. *Communications in Numerical Methods in Engineering*, 25(2), 185–200. <https://doi.org/10.1002/cnm.1119>
- Perkins, T., & Kern, L. R. (1961). Widths of hydraulic fractures. *Journal of Petroleum Technology*, 13(09), 937–949. <https://doi.org/10.2118/89-pa>
- Pruess, K. (2006). Enhanced geothermal systems (EGS) using CO₂ as working fluid—A novel approach for generating renewable energy with simultaneous sequestration of carbon. *Geothermics*, 35(4), 351–367. <https://doi.org/10.1016/j.geothermics.2006.08.002>
- Rahman, M., Hossain, M., & Rahman, S. (2002). A shear-dilation-based model for evaluation of hydraulically stimulated naturally fractured reservoirs. *International Journal for Numerical and Analytical Methods in Geomechanics*, 26(5), 469–497. <https://doi.org/10.1002/nag.208>
- Shimizu, H., Murata, S., & Ishida, T. (2011). The distinct element analysis for hydraulic fracturing in hard rock considering fluid viscosity and particle size distribution. *International Journal of Rock Mechanics and Mining Sciences*, 48(5), 712–727. <https://doi.org/10.1016/j.ijrmms.2011.04.013>
- Stanchits, S., Surdi, A., Gathogo, P., Edelman, E., & Suarez-Rivera, R. (2014). Onset of hydraulic fracture initiation monitored by acoustic emission and volumetric deformation measurements. *Rock Mechanics and Rock Engineering*, 47(5), 1521–1532. <https://doi.org/10.1007/s00603-014-0584-y>
- Van Mier, J. G., van Vliet, M. R., & Wang, T. K. (2002). Fracture mechanisms in particle composites: Statistical aspects in lattice type analysis. *Mechanics of Materials*, 34(11), 705–724. [https://doi.org/10.1016/s0167-6636\(02\)00170-9](https://doi.org/10.1016/s0167-6636(02)00170-9)
- Warpinski, N. R., Wolhart, S., & Wright, C. (2001). Analysis and prediction of microseismicity induced by hydraulic fracturing. In *SPE annual technical conference and exhibition*.
- Wilson, Z. A., & Landis, C. M. (2016). Phase-field modeling of hydraulic fracture. *Journal of the Mechanics and Physics of Solids*, 96, 264–290. <https://doi.org/10.1016/j.jmps.2016.07.019>
- Yan, C., Zheng, H., Sun, G., & Ge, X. (2016). Combined finite-discrete element method for simulation of hydraulic fracturing. *Rock Mechanics and Rock Engineering*, 49(4), 1389–1410. <https://doi.org/10.1007/s00603-015-0816-9>

- Yousefi, A., & Ng, T.-T. (2017). Dimensionless input parameters in discrete element modeling and assessment of scaling techniques. *Computers and Geotechnics*, 88, 164–173. <https://doi.org/10.1016/j.compgeo.2017.03.017>
- Zeng, Z., & Roegiers, J.-C. (2002). Experimental observation of injection rate influence on the hydraulic fracturing behavior of a tight gas sandstone. In *SPE/ISRM rock mechanics conference*.
- Zhao, X., Huang, B., & Xu, J. (2019). Experimental investigation on the characteristics of fractures initiation and propagation for gas fracturing by using air as fracturing fluid under true triaxial stresses. *Fuel*, 236, 1496–1504. <https://doi.org/10.1016/j.fuel.2018.09.135>
- Zhu, W., He, X., Li, Y., Lei, G., Santoso, R., & Wang, M. (2022). Impacts of fracture properties on the formation and development of stimulated reservoir volume: A global sensitivity analysis. *Journal of Petroleum Science and Engineering*, 217, 110852. <https://doi.org/10.1016/j.petrol.2022.110852>
- Zhuang, L., Kim, K. Y., Jung, S. G., Diaz, M., & Min, K.-B. (2019). Effect of water infiltration, injection rate and anisotropy on hydraulic fracturing behavior of granite. *Rock Mechanics and Rock Engineering*, 52(2), 575–589. <https://doi.org/10.1007/s00603-018-1431-3>